COMMUNICATION

Check for updates

A magnetron sputtered Mo₃Si thin film: an efficient electrocatalyst for N₂ reduction under ambient conditions†

Ting Wang, [ID] ab Qian Liu, [ID] b Tingshuai Li,b Siyu Lu, [ID] c Guang Chen, [ID] d Xifeng Shi,e Abdullah M. Asiri, [ID] f Yonglan Luo, [ID] *a Dongwei Ma [ID] *g and Xuping Sun [ID] *b

Industrially, large-scale NH₃ production mainly depends on the Haber−Bosch process, which is accompanied by heavy greenhouse gas emission and serious energy consumption. Electrochemical N₂ reduction is considered a sustainable strategy to solve this problem. Herein, we report for the first time that a Mo₃Si thin film sputtered on graphite paper is a favorable electrocatalyst for NH₃ synthesis under ambient conditions. Electrochemical tests suggest a large NH₃ yield rate of 2×10^{-10} mol s⁻¹ cm⁻² and a high Faraday efficiency of 6.69% at −0.4 V and −0.3 V *vs.* a reversible hydrogen electrode, respectively, in 0.1 M Na₂SO₄. It also demonstrates the high electrochemical and structural stability of such a catalyst as well as excellent selectivity for NH₃ generation. Density functional theory calculation reveals that the synergy of the metallic conductivity of Mo₃Si and the high chemical activity of the exposed Mo ions benefits the adsorption and activation of N₂, and a further proton−electron transfer reaction to produce NH₃.

As a significant chemical raw material, NH₃ is not only widely applied for the fabrication of resin, dyes, and explosives, but also considered as an attractive carbon-neutral energy carrier (17.7 wt% hydrogen content and 3 kW h kg⁻¹ energy density).[1–3] Currently, the industrial-scale technology of artificial synthetic NH₃ mainly depends on the Haber–Bosch process, which operates under harsh conditions, leading to serious carbon emission and great energy consumption.[4] Electrochemical N₂ reduction provides an alternative route for NH₃ synthesis in an environmentally benign and sustainable manner, but fairly the inertness of the strong N≡N triple bonds makes the reaction of N₂ fixation still a challenge.[5–11] Although a variety of noble metal-based electrocatalysts (Ag,[12] Au,[13,14] Pd,[15,16] and Ru[17]) perform effectively to drive the N₂ reduction reaction (NRR), their large-scale practical applications are still restricted due to their scarcity and expensiveness. As such, it is of great importance to design and develop earth-abundant alternatives.[18–36]

In nature, molybdenum (Mo) is involved in biological N₂ fixation with nitrogenase catalysis under mild conditions.[37–39] Additionally, Mo has also been proven to be a promising metal for the homogeneous NH₃ functionalization reaction.[40–45] However, It is challenging to graft such a catalyst onto electrodes for electrochemical tests.[46] Mo-based heterogeneous electrocatalysts can solve this issue, including Mo nanofilms,[47] MoS₂,[48] Mo₂C,[49] MoO₃,[50] MoN,[51] *etc.* Despite achieving some progress, the search and identification of new Mo-based heterogeneous electrocatalysts for efficient N₂-to-NH₃ fixation is still worth exploring.

Transition metal silicides as intermetallic compounds have specific crystal and electronic structures, which are different from those of their component metals.[52] As new catalytic materials, metal silicides have attracted growing attention by virtue of their unique physical and chemical properties, such as high thermal stability and electrical conductivity,[53,54] but their use for electrocatalytic N₂ reduction has not been reported before. Herein, we report on the development of a Mo₃Si thin film on graphite paper (Mo₃Si/GP) by direct current magnetron sputtering for the NRR. When tested in 0.1 M Na₂SO₄, the resulting Mo₃Si/GP achieves a large NH₃ yield rate of 2×10^{-10} mol s⁻¹ cm⁻² and a high Faraday efficiency (FE) of 6.69% at −0.4 V and −0.3 V *vs.* a reversible hydrogen electrode (RHE),

ᵃChemical Synthesis and Pollution Control, Key Laboratory of Sichuan Province, School of Chemistry and Chemical Engineering, China West Normal University, Nanchong 637002, Sichuan, China. E-mail: luoylcwnu@hotmail.com

ᵇInstitute of Fundamental and Frontier Sciences, University of Electronic Science and Technology of China, Chengdu 610054, Sichuan, China. E-mail: xpsun@uestc.edu.cn

ᶜGreen Catalysis Center, College of Chemistry, Zhengzhou University, Zhengzhou 450001, Henan, China

ᵈThe Key Laboratory of Life-Organic Analysis, Key Laboratory of Pharmaceutical Intermediates and Analysis of Natural Medicine, School of Chemistry and Chemical Engineering, Qufu Normal University, Qufu 273165, Shandong, China

ᵉCollege of Chemistry, Chemical Engineering and Materials Science, Shandong Normal University, Jinan 250014, Shandong, China

ᶠChemistry Department, Faculty of Science & Center of Excellence for Advanced Materials Research, King Abdulaziz University, P.O. Box 80203, Jeddah 21589, Saudi Arabia

ᵍKey Laboratory for Special Functional Materials of Ministry of Education, School of Materials Science and Engineering, Henan University, Kaifeng 475004, Henan, China. E-mail: dwmachina@126.com

† Electronic supplementary information (ESI) available. See DOI: 10.1039/d0ta11231c

respectively. Meantime, it also shows high electrochemical and structural stability. The possible NRR catalytic mechanism is also studied by density functional theory (DFT) calculations.

The X-ray diffraction (XRD) pattern of Mo_3Si in Fig. 1a shows two obvious diffraction peaks at 41.34° and 65.78° indexed to the (210) and (222) crystal planes of Mo_3Si (PDF # 97-064-4417), respectively. The scanning electron microscopy (SEM) image shows the formation of a Mo_3Si film on GP (Fig. 1b). Fig. S1† shows the cross-sectional SEM image of Mo_3Si, demonstrating that this film is thin in nature with a thickness of about 800 nm. As shown in Fig. 1d, the high-resolution transmission electron microscopy (HRTEM) image taken from the product (Fig. 1c) reveals an interplanar spacing of 0.214 nm indexed to the (210) plane of Mo_3Si. The crystalline nature of the Mo_3Si thin film is further supported by the selected area electron diffraction (SAED) pattern as shown in Fig. 1e. The scanning TEM (STEM) (Fig. 1f) and corresponding energy-dispersive X-ray (EDX) elemental mapping images conclude the uniform distribution of Mo and Si elements in the Mo_3Si thin film. Fig. 1g and h show the X-ray photoelectron spectroscopy (XPS) spectra of Mo_3Si in the Mo 3d and Si 2p regions, respectively. For Mo 3d, the banding energy (BE) peaks at 228.2 and 231.5 eV correspond to Mo $3d_{5/2}$ and Mo $3d_{3/2}$, respectively.[55] For Si 2p, the BE peak at 97.7 eV can be attributed to the Mo–Si bond while the other peak at 101.6 eV is associated with the Si–Si bond.[56]

The electrocatalytic NRR performance of Mo_3Si/GP (Mo_3Si mass loading: 0.4 mg cm^{-2}) was tested in 0.1 M Na_2SO_4 using a two-compartment electrochemical cell separated by a piece of Nafion 117 membrane, in which Mo_3Si/GP, Ag/AgCl, and a graphite rod were used as the working electrode, reference electrode, and counter electrode, respectively. All potentials were calibrated to an RHE scale. The produced NH_3 was spectrophotometrically determined by the indophenol blue method,[57] and the possible by-product N_2H_4 was detected by spectrophotometry using the Watt and Chrisp method.[58] Their detecting calibration curves are displayed in Fig. S2 and S3.† The linear sweep voltammetry curves in a N_2-and Ar-saturated 0.1 M Na_2SO_4 electrolyte (Fig. S5†) were used to estimate the range of potentials of Mo_3Si/GP for the NRR. Fig. 2a exhibits the time-dependent current density curves of Mo_3Si/GP at a series of potentials from −0.3 V to −0.7 V. After electromeasurements, the electrolytes were colored with the indophenol indicator in a light-shielded circumstance for 1 h and the UV-Vis absorption spectra of the electrolytes are shown in Fig. 2b. Its average NH_3 yield rate and the corresponding FEs at various potentials are plotted in Fig. 2c, which suggests that Mo_3Si/GP attains the largest NH_3 yield rate of 2×10^{-10} mol s^{-1} cm^{-2} and the highest FE of 6.69% at −0.4 V and −0.3 V, respectively, outperforming most reported NRR electrocatalysts listed in Table S1.† We also used ion chromatography to provide a reliable result in Fig. S5† for the quantitative of NH_3. When the potential becomes more negative, the HER becomes dominant, resulting in a decreased NH_3 yield rate and FE for the
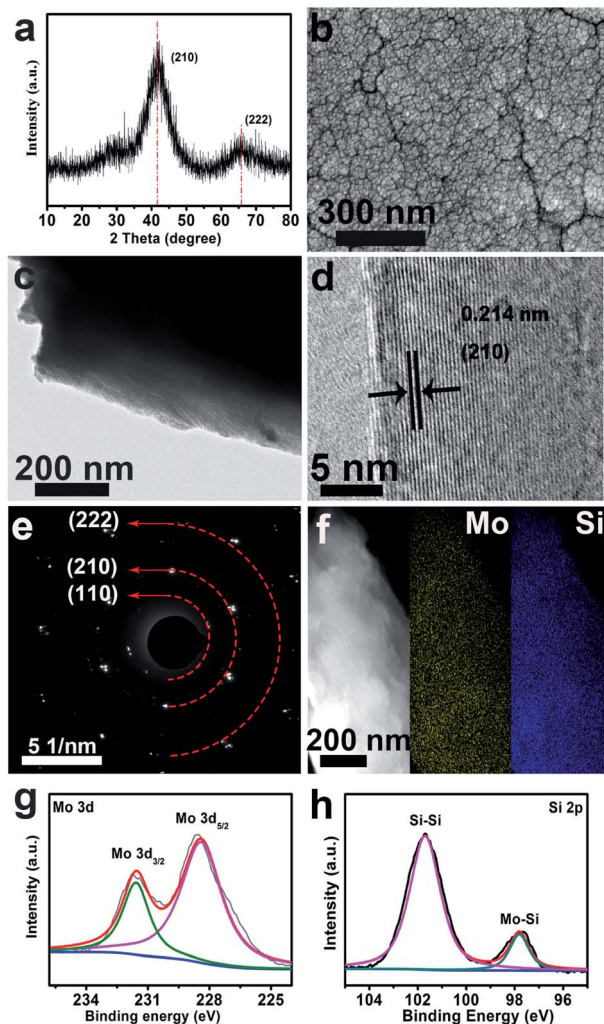

Fig. 1 (a) XRD pattern and (b) SEM image of Mo_3Si/GP. (c) TEM image, (d) HRTEM image, and (e) SAED pattern of Mo_3Si. (f) STEM and corresponding EDX elemental mapping images of Mo and Si of Mo_3Si. XPS spectra of Mo_3Si in the (g) Mo 3d and (h) Si 2p regions.
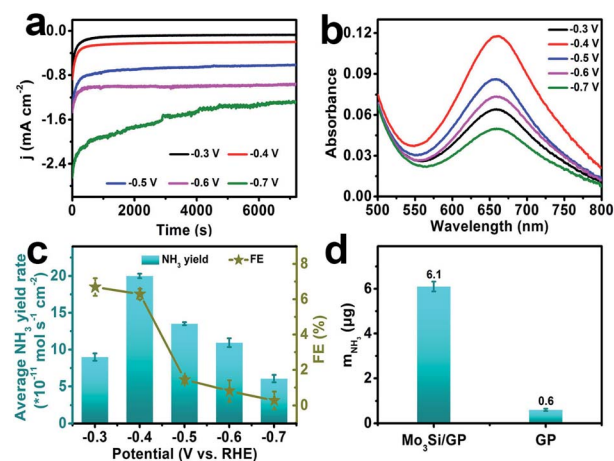

Fig. 2 (a) Time-dependent current density curves of Mo_3Si/GP at different potentials in 0.1 M Na_2SO_4. (b) UV-Vis absorption spectra of the electrolytes stained with the indophenol indicator after electrolysis at a series of potentials for 2 h. (c) Corresponding average NH_3 yield rate and FEs of Mo_3Si/GP at all potentials. (d) Amount of NH_3 produced for Mo_3Si/GP and GP after charging at −0.4 V for 2 h in 0.1 M Na_2SO_4.

This journal is © The Royal Society of Chemistry 2021

J. Mater. Chem. A, 2021, **9**, 884–888 | **885**

NRR.[59,60] Meanwhile, the possible by-product N_2H_4 is not detected (Fig. S6†), reflecting the excellent selectivity of Mo_3Si/GP for NH_3 synthesis. As shown in Fig. 2d, GP obtains a small amount of NH_3 (0.6 μg), while Mo_3Si/GP acquires a remarkable amount of NH_3 (6.1 μg) under the same conditions, suggesting that Mo_3Si/GP is highly active for the NRR.

To investigate the origin of the produced NH_3, we also performed a series of control experiments. As shown in Fig. 3a, the experiments were conducted in an Ar-saturated 0.1 M Na_2SO_4 electrolyte at −0.4 V and a N_2-saturated 0.1 M Na_2SO_4 electrolyte at open-circuit potential. As expected, almost no NH_3 is detected and the corresponding UV-Vis absorption spectra are exhibited in Fig. S7.† Moreover, we performed the alternative N_2-saturated and Ar-saturated tests at −0.4 V for 2 h in 0.1 M Na_2SO_4. As shown in Fig. 3b, the amount of NH_3 detected in the Ar-saturated electrolyte is negligible compared to that in the N_2-saturated electrolyte. Both results indicate that the NH_3 products are mainly generated from Mo_3Si/GP electrocatalysis. Besides, stability is another crucial parameter for electrocatalysts. As shown in Fig. 3c, after 6 consecutive cycle tests, both the NH_3 yield rate and FEs exhibit almost no obvious decline. The corresponding time-dependent current density curves and UV-Vis absorption spectra are displayed in Fig. S8.† Besides, this catalyst can maintain its catalytic activity for at least 26 h (Fig. 3d). Almost no ammonia was detected in the anodic electrolytes stained with the indophenol indicator (Fig. S9†). Furthermore, the photographs of pH test papers of the 0.1 M Na_2SO_4 aqueous solution before and after 2 h electrolysis indicate that there is almost no obvious change of pH in our experiment (Fig. S10†). These data suggest the excellent electrochemical durability of Mo_3Si/GP. After a long-term NRR, the XRD analysis confirms that this catalyst is still Mo_3Si/GP in nature (Fig. S11†), and the SEM image shows that this catalyst also maintains its thin film morphology (Fig. S12†). As shown in Fig. S13,† after electrolysis, there is no obvious change in the XPS spectra of Mo_3Si in the Mo 3d and Si 2p regions.
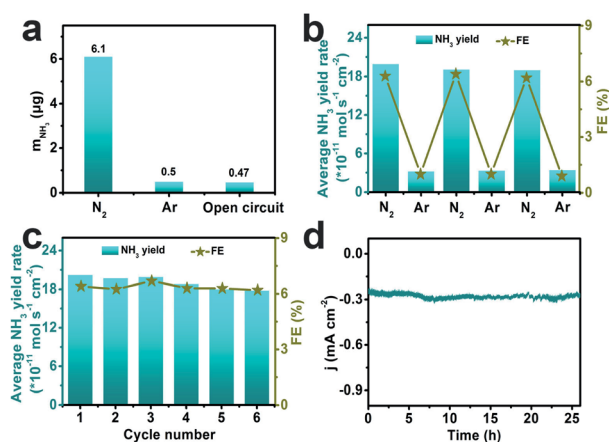
To gain fundamental insights into the NRR mechanism of the Mo_3Si catalyst, first-principles calculations based on DFT have been performed, and the relevant computational details are presented in the ESI.† The unit cell of Mo_3Si and its density of states (DOS) are presented in Fig. S14.† The calculated lattice parameter of 4.84 Å (Fig. S14a†) is in good agreement with the experimental value of 4.91 Å.[61] The plenty electronic states around the Fermi level (Fig. S14b†) show the metallic conductivity of Mo_3Si, which facilitates the electron transfer during the NRR process. To be specific, the Mo_3Si (210) surfaces have been studied for the NRR, which is the most abundant according to the XRD and HRTEM characterization. The Mo_3Si (210) (2 × 1) supercell and its DOS are shown in Fig. S15.† As shown in Fig. S15a,† various potential adsorption sites for N_2 molecules have been considered. The obtained stable adsorption configurations are displayed in Fig. S16.† It is noted that for all the adsorption configurations the N_2 molecules are chemisorbed with significantly negative adsorption energies, ranging from −1.55 to −0.71 eV, and the Mo atoms of the support serve as the active sites. Especially, the configurations in Fig. S16a and b,† denoted as N_2^α and N_2^β, respectively, are much more thermodynamically favorable than others, for both of which the N_2 molecules are bonded with three Mo atoms. Therefore, in the following we studied the NRR on the Mo_3Si (210) surface for the N_2^α and N_2^β configurations.

The calculated NRR free energy diagrams together with the charge density differences for the N_2^α and N_2^β configurations are presented in Fig. 4a and b, respectively. The reaction intermediates are displayed in Fig. S17 and S18.† The charge density differences in the insets of Fig. S14† suggest that N_2 adsorption on the Mo_3Si (210) surface follows the "acceptance-donation" mechanism. It is noted that, due to the high chemical activity of Mo, N_2 can be strongly activated, as indicated by the significant elongation of the N–N bond (larger than 1.2 Å), and the significant transfer of electrons from the support to the N_2 (larger than 1e). There are several well-established reaction pathways for the NRR depending on the specific adsorption modes of N_2 molecules.[62–64] For the side-on configurations herein, the NRR can proceed through a consecutive or an enzymatic pathway. Thanks to the strong activation of N_2, its hydrogenation needs a tiny energy, 0.10 and 0.04 eV, respectively, for N_2^α and N_2^β configurations. Furthermore, it is found that the enzymatic pathway is energetically much more favorable than the consecutive one, given that for the second hydrogenation step *NH–*NH is more stable than *N–*NH$_2$ by ∼0.5 eV. Therefore, we only studied the enzymatic pathway, as presented in Fig. S14.† Importantly, for both N_2^α and N_2^β configurations, the potential-determining step is the last hydrogenation step to produce the second NH_3 molecule, giving a limiting potential of −0.43 V, close to the experimentally optimal working potential (−0.3 or −0.4 V). In addition, H adsorption has been studied to evaluate the NRR selectivity against the HER. From Fig. S19,† the active sites for the NRR can also effectively bind H atoms. However, compared with the N_2 adsorption, the H adsorption is less stable by more than 0.5 eV. Thus, the Mo_3Si (210) surface prefers to adsorb N_2 molecules rather than H, which provides a high NRR selectivity, in good agreement with the high FE

Fig. 3 (a) The amount of NH_3 produced for Mo_3Si/GP under different electrochemical conditions. (b) NH_3 yield rate of alternative N_2-saturated and Ar-saturated tests at −0.4 V for 2 h. (c) NH_3 yield rate and FE of cycling tests at −0.4 V. (d) Time-dependent current density curve of Mo_3Si/GP at −0.4 V for 26 h.

886 | *J. Mater. Chem. A*, 2021, **9**, 884–888

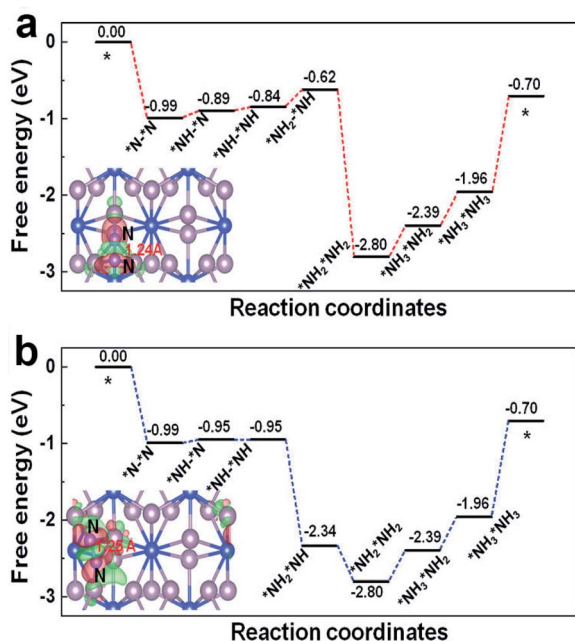This journal is © The Royal Society of Chemistry 2021

Fig. 4 The free energy (in eV) diagrams for the NRR on the Mo$_3$Si (210) (2 × 1) surface at zero potential through the enzymatic pathway. (a) and (b) are for N$_2^\alpha$ and N$_2^\beta$ configurations presented in Fig. S16a and b,† respectively. The calculated charge density difference for N$_2^\alpha$ and N$_2^\beta$ are presented as insets, where red and green shadows represent the charge accumulation and loss, respectively. The positions of the N atoms are roughly marked. The blue and mauve spheres denote the Si and Mo atoms, respectively.

observed experimentally. Overall, the calculation results indicate that the synergy of the metallic conductivity of Mo$_3$Si and the high chemical activity of Mo ions plays an important role in the adsorption and activation of N$_2$, and a further proton–electron transfer reaction to produce NH$_3$.

In summary, Mo$_3$Si has been proven as a stable and active NRR electrocatalyst with a large NH$_3$ yield rate of 2×10^{-10} mol s^{-1} cm^{-2} and a high FE of 6.69% at −0.4 V and −0.3 V vs. RHE, respectively, in neutral media. This work not only provides us an attractive earth-abundant catalyst material for NH$_3$ electrosynthesis under ambient conditions, but would also open up a new avenue to fabricate catalyst films via magnetron sputtering for N$_2$-fixation applications.[65]

Conflicts of interest

There are no conflicts to declare.

Acknowledgements

References

1 V. Smil, Nature, 1999, 400, 415.

2 A. Klerke, C. H. Christensen, J. K. Nørskov and T. Vegge, J. Mater. Chem., 2008, 18, 2304–2310.

3 R. Schlçgl, Angew. Chem., Int. Ed., 2003, 42, 2004–2008.

4 I. Dybkjaer, in Ammonia, catalysis and manufacture, ed. A. Nielsen, Springer, Heidelberg, 1995, pp. 199–308.

5 C. J. M. van der Ham, M. T. M. Koper and D. G. H. Hetterscheid, Chem. Soc. Rev., 2014, 43, 5183–5191.

6 X. Zhu, S. Mou, Q. Peng, Q. Liu, Y. Luo, G. Chen, S. Gao and X. Sun, J. Mater. Chem. A, 2020, 8, 1545–1556.

7 B. Ma, H. Zhao, T. Li, Q. Liu, Y. Luo, C. Li, S. Lu, A. M. Asiri, D. Ma and X. Sun, Nano Res., 2020, DOI: 10.1007/s12274-020-3049-5.

8 V. Kyriakou, I. Garagounis, E. Vasileiou, A. Vourros and M. Stoukides, Catal. Today, 2017, 286, 2–13.

9 C. Guo, J. Ran, A. Vasileff and S. Qiao, Energy Environ. Sci., 2018, 11, 45–56.

10 M. D. Fryzuk, J. B. Love, S. J. Rettig and V. G. Young, Science, 1997, 275, 1445–1447.

11 H. Jia and E. A. Quadrelli, Chem. Soc. Rev., 2014, 43, 547–564.

12 H. Huang, L. Xia, X. Shi, A. M. Asiri and X. Sun, Chem. Commun., 2018, 54, 11427–11430.

13 S. Li, D. Bao, M. Shi, B. Wulan, J. Yan and Q. Jiang, Adv. Mater., 2017, 29, 1700001.

14 M. Nazemi, S. R. Panikkanvalappil and M. A. El-Sayed, Nano Energy, 2018, 49, 316–323.

15 J. Wang, L. Yu, L. Hu, G. Chen, H. Xin and X. Feng, Nat. Commun., 2018, 9, 1795.

16 G. Deng, T. Wang, A. A. Alshehri, K. A. Alzahrani, Y. Wang, H. Ye, Y. Luo and X. Sun, J. Mater. Chem. A, 2019, 7, 21674–21677.

17 Z. Geng, Y. Liu, X. Kong, P. Li, K. Li, Z. Liu, J. Du, M. Shu, R. Si and J. Zeng, Adv. Mater., 2018, 30, 1803498.

18 T. Wu, H. Zhao, X. Zhu, Z. Xing, Q. Liu, T. Liu, S. Gao, S. Lu, G. Chen, A. M. Asiri, Y. Zhang and X. Sun, Adv. Mater., 2020, 32, 2000299.

19 T. Xu, D. Ma, T. Li, L. Yue, Y. Luo, S. Lu, A. M. Asiri, C. Yang and X. Sun, Chem. Commun., 2020, 56, 14031–14034.

20 S. Gao, Y. Zhu, Y. Chen, M. Tian, Y. Yang, T. Jiang and Z. Wang, Mater. Today, 2019, 28, 17–24.

21 P. Wei, Q. Geng, A. I. Channa, X. Tong, Y. Luo, S. Lu, G. Chen, S. Gao, Z. Wang and X. Sun, Nano Res., 2020, 13, 2967–2972.

22 L. Li, C. Tang, B. Xia, H. Jin, Y. Zheng and S. Qiao, ACS Catal., 2019, 9, 2902–2908.

23 Y. Liu, M. Han, Q. Xiong, S. Zhang, C. Zhao, W. Gong, G. Wang, H. Zhang and H. Zhao, Adv. Energy Mater., 2019, 9, 1803935.

24 C. Li, J. Yu, L. Yang, J. Zhao, W. Kong, T. Wang, A. M. Asiri, Q. Li and X. Sun, Inorg. Chem., 2019, 58, 9597–9601.

25 L. Zhang, L. Ding, G. Chen, X. Yang and H. Wang, Angew. Chem., Int. Ed., 2019, 58, 2612–2616.

26 C. Li, D. Ma, S. Mou, Y. Luo, B. Ma, S. Lu, G. Cui, Q. Li, Q. Liu and X. Sun, J. Energy Chem., 2020, 50, 402–408.

27 Y. Wang, M. Shi, D. Bao, F. Meng, Q. Zhang, Y. Zhou, K. Liu, Y. Zhang, J. Wang, Z. Chen, D. Liu, Z. Jiang, M. Luo, L. Gu, Q. Zhang, X. Cao, Y. Yao, M. Shao, Y. Zhang, X. Zhang,

This journal is © The Royal Society of Chemistry 2021

J. Mater. Chem. A, 2021, 9, 884–888 | 887

J. Chen, J. Yan and Q. Jiang, *Angew. Chem., Int. Ed.*, 2019, **58**, 9464–9469.

28 X. Lv, F. Wang, J. Du, Q. Liu, Y. Luo, S. Lu, G. Chen, S. Gao, B. Zheng and X. Sun, *Sustainable Energy Fuels*, 2020, **4**, 4469–4472.

29 C. Lv, C. Yan, G. Chen, Y. Ding, J. Sun, Y. Zhou and G. Yu, *Angew. Chem., Int. Ed.*, 2018, **57**, 6073–6076.

30 R. Zhao, Q. Geng, L. Chang, P. Wei, Y. Luo, X. Shi, A. M. Asiri, S. Lu, Z. Wang and X. Sun, *Chem. Commun.*, 2020, **56**, 9328–9331.

31 Q. Qin, Y. Zhao, M. Schmallegger, T. Heil, J. Schmidt, R. Walczak, G. Demner, H. Jiao and M. Oschatz, *Angew. Chem., Int. Ed.*, 2019, **58**, 13101–13106.

32 T. Wang, S. Li, B. He, X. Zhu, Y. Luo, Q. Liu, T. Li, S. Lu, C. Ye, A. M. Asiri and X. Sun, *Chin. J. Catal.*, 2021, **42**, 1024–1029.

33 K. Chu, Y. Liu, Y. Li, J. Wang and H. Zhang, *ACS Appl. Mater. Interfaces*, 2019, **11**, 31806–31815.

34 X. Cheng, J. Wang, W. Xiong, T. Wang, T. Wu, S. Lu, G. Chen, S. Gao, X. Shi, Z. Jiang, X. Niu and X. Sun, *ChemNanoMat*, 2020, **6**, 1315–1319.

35 L. Huang, J. Wu, P. Han, A. M. Al-Enizi, T. M. Almutairi, L. Zhang and G. Zheng, *Small Methods*, 2019, **3**, 1800386.

36 J. Gao, X. Lv, F. Wang, Y. Luo, S. Lu, G. Chen, S. Gao, B. Zhong, X. Guo and X. Sun, *J. Mater. Chem. A*, 2020, **8**, 17956–17959.

37 B. M. Hoffman, D. Lukoyanov, Z. Yang, D. Dean and L. C. Seefeldt, *Chem. Rev.*, 2014, **114**, 4041–4062.

38 S. F. McWilliams and P. L. Holland, *Acc. Chem. Res.*, 2015, **48**, 2059–2065.

39 L. C. Seefeldt, B. M. Hoffman and D. R. Dean, *Annu. Rev. Biochem.*, 2009, **78**, 701–722.

40 L. A. Wickramasinghe, T. Ogawa, R. R. Schrock and P. Muller, *J. Am. Chem. Soc.*, 2017, **139**, 9132–9135.

41 M. Yu, T. Ogawa, S. R. R. chrock and A. H. Hoveyda, *Angew. Chem., Int. Ed.*, 2015, **54**, 215–220.

42 R. R. Eady, *Chem. Rev.*, 1996, **96**, 3013–3030.

43 R. R. Schrock, *Acc. Chem. Res.*, 2005, **38**, 955–962.

44 H. Tanaka, Y. Nishibayashi and K. Yoshizawa, *Acc. Chem. Res.*, 2016, **49**, 987–995.

45 K. Arashiba, E. Kinoshita, S. Kuriyama, A. Eizawa, K. Nakajima, H. Tanaka, K. Yoshizawa and Y. Nishibayashi, *J. Am. Chem. Soc.*, 2015, **137**, 5666–5669.

46 E. S. Andreiadis, P.-A. Jacques, P. D. Tran, A. Leyris, M. Chavarot-Kerlidou, B. Jousselme, M. Matheron, J. Pécaut, S. Palacin, M. Fontecave and V. Artero, *Nat. Chem.*, 2013, **5**, 48–53.

47 D. Yang, T. Chen and Z. Wang, *J. Mater. Chem. A*, 2017, **5**, 18967–18971.

48 Y. Liu, M. Han, Q. Xiong, S. Zhang, C. Zhao, W. Gong, G. Wang, H. Zhang and H. Zhao, *Adv. Energy Mater.*, 2019, **9**, 1803935.

49 H. Cheng, L. Ding, G. Chen, L. Zhang, J. Xue and H. Wang, *Adv. Mater.*, 2018, **30**, 1803694.

50 J. Han, X. Ji, X. Ren, G. Cui, L. Li, F. Xie, H. Wang, B. Li and X. Sun, *J. Mater. Chem. A*, 2018, **6**, 12974–12977.

51 L. Zhang, X. Ji, X. Ren, Y. Luo, X. Shi, A. M. Asiri, B. Zheng and X. Sun, *ACS Sustainable Chem. Eng.*, 2018, **6**, 9550–9554.

52 M. E. Schlesinger, *Chem. Rev.*, 1990, **90**, 607–628.

53 S. P. Murarka, *Annu. Rev. Mater. Sci.*, 1983, **13**, 117–137.

54 X. Chen and C. Liang, *Catal. Sci. Technol.*, 2019, **9**, 4785–4820.

55 X. Zhu, X. Jiang, X. Yao, Y. Leng, L. Wang and Q. Xue, *ACS Appl. Mater. Interfaces*, 2019, **11**, 26880–26890.

56 C. Deng, Y. Wang, B. He, W. Zhang, F. Dang, H. Wang and Y. Du, *J. Mater. Chem. A*, 2020, **8**, 259–267.

57 D. Zhu, L. Zhang, R. E. Ruther and R. J. Hamers, *Nat. Mater.*, 2013, **12**, 836–841.

58 G. W. Watt and J. D. Chrisp, *Anal. Chem.*, 1952, **24**, 2006–2008.

59 X. Ren, J. Zhao, Q. Wei, Y. Ma, H. Guo, Q. Liu, Y. Wang, G. Cui, A. M. Asiri, B. Li, B. Tang and X. Sun, *ACS Cent. Sci.*, 2019, **5**, 116–121.

60 W. Qiu, X. Xie, J. Qiu, W. Fang, R. Liang, X. Ren, X. Ji, G. Cui, A. M. Asiri, G. Cui, B. Tang and X. Sun, *Nat. Commun.*, 2018, **9**, 3485.

61 A. Misra, J. J. Petrovic and T. E. Mitchell, *Scr. Mater.*, 1998, **40**, 191–196.

62 D. Ma, Z. Zeng, L. Liu, X. Huang and Y. Jia, *J. Phys. Chem. C*, 2019, **123**, 19066–19076.

63 X. Liu, Y. Jiao, Y. Zheng, M. Jaroniec and S.-Z. Qiao, *J. Am. Chem. Soc.*, 2019, **141**, 9664–9672.

64 D. Ma, Z. Zeng, L. Liu and Y. Jia, *J. Energy Chem.*, 2021, **54**, 501–509.

65 F. Wang, H. Zhao, J. Liang, T. Li, Y. Luo, S. Lu, X. Shi, B. Zheng, J. Du and X. Sun, *J. Mater. Chem. A*, 2020, **8**, 20260–20285.